ACS APPLIED ELECTRONIC MATERIALS

pubs.acs.org/acsaelm

Article

Pixel-Level Image-Based Analysis of Spatial Kinetics and Resistance Variation in a Large-Area Electrochromic Device

Shifa Sarkar, Takefumi Yoshida, Banchhanidhi Prusti, Satya Ranjan Jena, Kuo-Chuan Ho, and Masayoshi Higuchi*

Cite This: *ACS Appl. Electron. Mater.* 2025, 7, 10651−10663

Read Online

ACCESS | Metrics & More | Article Recommendations | Supporting Information

ABSTRACT: Electrochromic (EC) materials and devices (ECDs) have been extensively studied, providing valuable insight into their optical switching properties and material characteristics. To analyze dynamic and subtle spatial variations during switching, we developed for the first time a noninvasive, automated, image-based methodology capable of resolving EC behavior at the pixel level. Grayscale images, extracted from video recordings at 0.0333 s intervals during cyclic operation, were segmented into 8,448 localized pixel positions to quantify contrast−time profiles. First, switching nonuniformity was visualized, revealing reaction times from 0.8 to 2.0 s to reach 90% contrast change, with faster responses at the edges and slower transitions in the center. Second, segmental kinetics were evaluated by fitting time constants (τ) to each profile and linking them to composite resistances using a simplified RC model with a uniform areal capacitance (0.0133 F cm^{-2}). The edge segment exhibited lower τ (1.79) and resistance (134.5 $\Omega \cdot cm^2$), whereas the central pixel position showed delayed switching (1.80 s) with larger τ (2.46) and higher resistance (184.9 $\Omega \cdot cm^2$). Finally, spatial distributions were visualized through 2D heat maps, confirming slower central regions (1.60−1.95 s), with regional average resistance of 185.7 $\Omega \cdot cm^2$ compared to lower-resistance peripheral regions (136.8−149.6 $\Omega \cdot cm^2$). This noninvasive approach enables a high-resolution diagnostic platform for quantifying uniformity, kinetics, and resistance distributions in large-area ECDs and is broadly applicable to diverse EC architectures influenced by spatial transport effects.

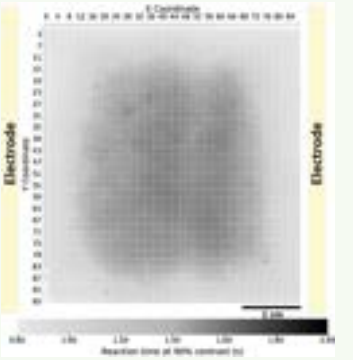

KEYWORDS: *metallo-supramolecular polymer, electrochromic device, Python Library, pixel values, image analysis*

INTRODUCTION

Electrochromic (EC) materials are characterized by their ability to reversibly change color or transparency when a voltage is applied, forming the basis for electrochromic devices (ECDs) that dynamically modulate optical properties such as color and transmittance under electrical stimulation.[1−3] Such devices have been developed to control the transmission or absorption of light, typically in the visible or near-infrared regions of the electromagnetic spectrum.[4−6] In recent years, ECDs have received growing attention due to their low power consumption characteristics, in addition to their flexibility and versatility in various applications, such as smart windows, information displays, e-papers, rearview mirrors, and even some types of eyewear.[7−11] An ECD comprises at least one EC active layer, an electrolyte, and transparent conductive electrodes.[12,13] The EC layer can include materials such as transition metal oxides (e.g., tungsten oxide), conducting polymers, or organic compounds.[14−18] Among the various EC materials reported to date, metallosupramolecular polymers (MSPs), such as Fe(II)-based MSP **polyFeL1**, have received growing attention due to their unique properties, such as high contrast ratios, fast response times, and excellent stabilities.[19−21]

The core concept underlying **polyFeL1**-based ECDs is the occurrence of reversible redox reactions inside the thin-film structure. When a voltage is applied across the device, ions or electrons are driven into or out of the EC material, causing a reversible change from a transparent state to a colored one, or from one colored state to another.[22,23] A methanolic solution of this Fe polymer is purple, wherein the color originates from the absorption of the metal-to-ligand charge transfer (MLCT) transition (i.e., from Fe(II) to the ligand) at a wavelength of ∼580 nm.[24,25] ECDs possess various benefits over conventional methods of controlling light and heat (e.g., mechanical blinds or curtains) since they can be precisely adjusted and respond fast to changes in the electrical signal.[26] In the case of a smart window, the EC material may change from a clear to a colorful or reflecting state, controlling the amount of light and heat that can pass through. Such dynamic control of the optical characteristics provides several benefits, including an improved

Received: August 25, 2025
Revised: November 1, 2025
Accepted: November 16, 2025
Published: November 21, 2025

energy efficiency, user comfort, glare reduction, privacy, and aesthetic appeal.[27−29] Understanding these properties therefore is crucial for analyzing the ECDs.

In the dynamic realm of materials science, data analytical methods are crucial tools for understanding, optimizing, and developing materials with remarkable efficiency and precision.[30] These methods include techniques such as statistical analysis and machine learning algorithms.[31,32] In the context of materials science research, visual data representation, such as in the form of pictures or videos, is essential because it allows researchers to directly observe and evaluate the characteristics and behaviors of materials, allowing them to discover hidden patterns.[33,34] Conventional methods for EC analysis in materials science predominantly rely on scanning electron microscopy, ultraviolet−visible (UV−vis) spectroscopy, and electrochemical impedance spectroscopy; have provided valuable insights into switching mechanisms and material properties.[14,35−39] Despite the widespread application of these traditional methods, they often exhibit limited spatial resolutions and require sophisticated instrumentation. For example, previous work on thermal degradation of ECDs using transmittance spectroscopy successfully monitored optical changes at 580 nm.[40] However, this approach was limited to a single wavelength, potentially omitting information regarding changes occurring in other parts of the spectrum. These limitations highlight the need for alternative data analysis strategies capable of providing spatially resolved, time-dependent information.

To address this challenge, this work reports a novel image-based analytical method for two-dimensional (2D) investigation of ECD using images and movie. This method is developed using the Python Library,[41−45] and is specifically designed to analyze grayscale images of ECDs, potentially rendering it an effective tool for quantitative investigation of the color-changing behavior of MSP-based ECDs. Notably, Python provides a robust image processing and analysis environment based on OpenCV (Open-Source Computer Vision Library).[46] More specifically, grayscale images represent variations in intensity using different shades of gray, while the pixel values in the grayscale images represent the intensity of light at each pixel,[47] thereby allowing changes in the optical properties to be monitored over time. Through this non-invasive and automated methodology, the aim is to analyze ECDs by tracking and quantifying EC changes at the pixel level. Consequently, this study aims to enhance our understanding of EC behavior, including their kinetics, uniformity, and spatial distributions.

EXPERIMENTAL SECTION

Materials and Instruments. All purchased chemicals and reagents were of analytical grade and were used as received without further purification. Poly(methyl methacrylate) (PMMA, M_w = 350 kg mol^{-1}) and the indium tin oxide (ITO)-coated glass substrate (resistivity 8−12 Ω/sq) were purchased from Sigma-Aldrich, USA. Methanol (MeOH) and propylene carbonate (PC) were obtained from Wako Pure Chemical Industries, Ltd., Japan, while lithium perchlorate ($LiClO_4$) and nickel hexacyanoferrate (NiHCF) were obtained from Kanto Chemical Co., Inc., Japan. The Fe(II)-based MSP (**polyFeL1**) was purchased from Tokyo Chemical Industry (TCI) Co., Ltd., Japan. Thermo Electron LED GmbH (Smart2Pure 6 UV) was purchased from Nikko Hansen & Co., Ltd., Japan, and used to prepare deionized water for the preparation of the counter material solution.

An Apeiros API Corporation (Tokyo) automated spray coater machine was used for preparing the **polyFeL1** and counter material films. An ESPEC Corp. benchtop-type chamber (SH-242) was used as the temperature and humidity control chamber. An ALS/CHI electrochemical workstation (CH Instruments, Inc.) was used as the potentiostat for all chronoamperometric measurements.

Spatiotemporal Image Acquisition. A VHX-970F digital microscope was used to capture movies and photographic images of the **polyFeL1**-based ECD during cycling. The microscope was equipped with a Z00 lens operated at ×5 magnification, and the exposure time (1/60 s) was synchronized with the 60 Hz LED illumination to prevent flicker and rolling-shutter artifacts. For kinetic analysis, frames corresponding to −1 to 3 s (120 frames in total) were analyzed, providing a 33 ms temporal resolution that was sufficient to resolve the EC switching behavior without motion blur or illumination distortion. The original microscope video was recorded at a resolution of 800 × 600 pixels. For image analysis, the EC active area (48 × 44 mm) was cropped as the region of interest, corresponding to 480 × 440 pixels in the length scale. After 5 × 5 pixel averaging, the final analytical grid contained 96 × 88 segments, yielding an effective spatial resolution of approximately 0.50 × 0.50 mm (0.25 mm^2) per segment, which defines the smallest unit analyzed for grayscale kinetics. In addition to spatial resolution, the temporal acquisition parameters were also optimized. Video acquisition was performed at 30 frames s^{-1}, corresponding to a temporal resolution of 0.0333 s per data point in the contrast−time plots. This frame rate was sufficient to capture the complete EC transition without distortion or loss of kinetic detail of the **polyFeL1**-based ECD. Increasing the frame rate did not alter the validity or spatial pattern of the extracted kinetics; therefore, 30 fps was adopted as an optimal setting for reliable and efficient image-based analysis. For devices exhibiting faster EC switching (≤1 s), a higher acquisition rate (e.g., 50 fps) is recommended to achieve improved temporal resolution.

Preparation of the PolyFeL1 and NiHCF Films on ITO-Glass Substrates. Initially, **polyFeL1** was dissolved in MeOH to prepare a 3 mg/mL polymer solution, which was subsequently filtered through a microsyringe (polyvinylidene fluoride, 0.45 μm) to eliminate any trace amounts of insoluble residue. The ITO-glass substrate was cleaned using acetone and treated with UV irradiation and ozone for 20 min prior to the preparation of the polymer film. After this time, the ITO-glass substrate was heated at 57−60 °C on a hot plate before spraying. More specifically, the automated spray coater was used to generate a uniform, smooth, and purple-colored **polyFeL1** coating on the ITO-glass substrate using the above-prepared polymer solution. The coating process was performed at 200 rpm, and a total of three coatings were applied to give the desired film.

Using the same procedure, a NiHCF thin film was prepared on another ITO-glass substrate. In this case, an aqueous solution of NiHCF (75 μL/mL) was employed, and the hot plate temperature was set to 93−95 °C, and a total of two coatings were applied to give the desired film thickness. The resulting material was used as the counter electrode.

Preparation of the Gel Electrolyte. $LiClO_4$ (0.3 g) and PC (2.0 mL) were added to a screw-neck vial and stirred for 20 min. Subsequently, PMMA (2.0 g) was added gradually with

https://doi.org/10.1021/acsaelm.5c01754
ACS Appl. Electron. Mater. 2025, 7, 10651−10663

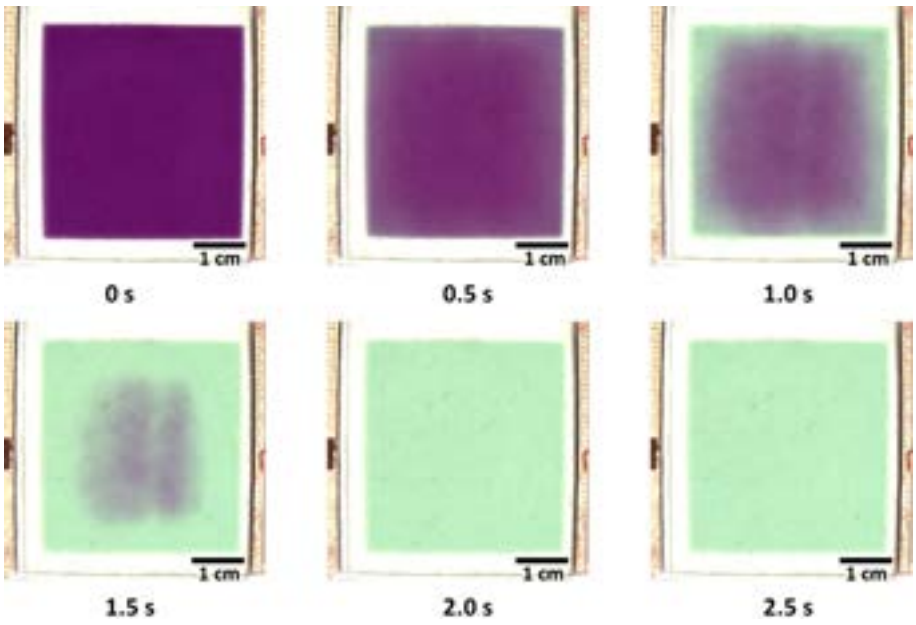

Figure 1. Movie capture in a **polyFeL1**-based ECD under an applied voltage of 1.2 V, showing the transition from colored (purple) to bleached (colorless) states over time (0−2.5 s).

vigorously stirring ($LiClO_4$/PC/PMMA = 8:46:46, wt %), and the resulting mixture was stirred under vacuum for 1 h at room temperature. After this time, a cloudy and viscous liquid electrolyte was obtained.

Device Fabrication. To prepare the solid-state **polyFeL1**-based ECD, the gel electrolyte was poured onto a **polyFeL1**-coated ITO-glass substrate (working electrode, WE, 5.0 × 5.0 cm^2) and covered by another ITO-glass substrate, which was coated with NiHCF (counter electrode, CE, 5.0 × 5.0 cm^2) to form a sandwich configuration solid-state device in which the electrodes were separated by the gel electrolyte. The resulting device was placed in a temperature/humidity control chamber, where the temperature was set to 95 °C and the relative humidity (RH) to 40%. Once the temperature of the chamber reached 95 °C, it was cooled to 25 °C at 80% RH. Finally, the device was cleaned, and a voltage (1.2 V) was applied to observe the color change (Scheme S1a).

The image-based analysis in this study was performed on a single representative **polyFeL1**-based ECD during its first EC switching cycle. Because the primary objective of this work is to establish and validate the image-based analytical methodology rather than to perform a statistical comparison among multiple devices, thus only one device was analyzed in detail.

RESULTS AND DISCUSSION

Movie Capture and Processing of Image Data. In the UV−vis spectrum of the prepared purple **polyFeL1** specimen, an absorption band appeared at ∼580 nm, which was attributed to the MLCT transition from Fe(II) to the ligand, and accounted for the purple color of the methanolic solution.[2,55] It was considered that upon subjecting Fe(II) to electrochemical oxidation upon the application of a voltage, Fe(III) would be generated, and the MLCT absorption band would be eliminated, leading to a change in color.[24] Importantly, it was observed that the fabricated **polyFeL1**-based ECD displayed reversible color changes from purple to colorless at low voltages of 1.2−0 V. More specifically, Figure 1 illustrates a time-dependent image sequence depicting the EC properties of the **polyFeL1**-based ECD under chronoamperometric analysis at a constant potential of 1.2 V over 3 s. Initially, the device appeared deep purple, transitioning to colorless as Fe^{2+} (original state) underwent electrochemical oxidation to Fe^{3+} (oxidized state) upon voltage application. The device exhibited a fast EC response, with complete decolorization being observed after 2.0 s (fifth image). However, the intermediate state at 1.0 and 1.5 s (third and fourth images) revealed nonuniform color transitions, with lighter edges and a purple color in the center, revealing variable regional response rates. This observed nonuniformity underscores the need for image data analysis to capture spatial and temporal variations in the optical response of ECDs.

To develop the new analytical method, movie of the **polyFeL1**-based ECD was captured using a digital microscope equipped with an appropriate Z00 lens at × 5 magnification to focus on the display surface and record the color-changing property of the device during the switching process (Scheme S1b). The complete camera setting was provided in Table S1. Using the Python Library, image data were collected from the movie at a regular interval of 0.0333 s (≈30 fps). From these original images, the region of interest (ROI) was selected and cropped, and the cropped images were converted into grayscale images. In this work, grayscale contrast values were expressed on an 8-bit scale, where 0 represents black and 255 represents white, obtained through OpenCV's standard conversion (cv2.cvtColor). For example, a value of 30 indicates a dark gray region, while 240 corresponds to a light gray area, directly representing the optical brightness in the standardized grayscale image. A total of 211,200 pixels were extracted from the grayscale images, and adjacent pixel values were merged to obtain a single segment for every 25 (5 × 5) pixels. This segmentation step was essential to reduce data noise, smooth local intensity fluctuations, and improve the reliability of contrast−time analysis across the device. Additionally, aggregating pixel data into segments allowed manageable computation while retaining sufficient spatial resolution to capture meaningful switching behavior. After averaging the

https://doi.org/10.1021/acsaelm.5c01754
ACS Appl. Electron. Mater. 2025, 7, 10651−10663

Scheme 1. Processing the Image Data using the Python Library

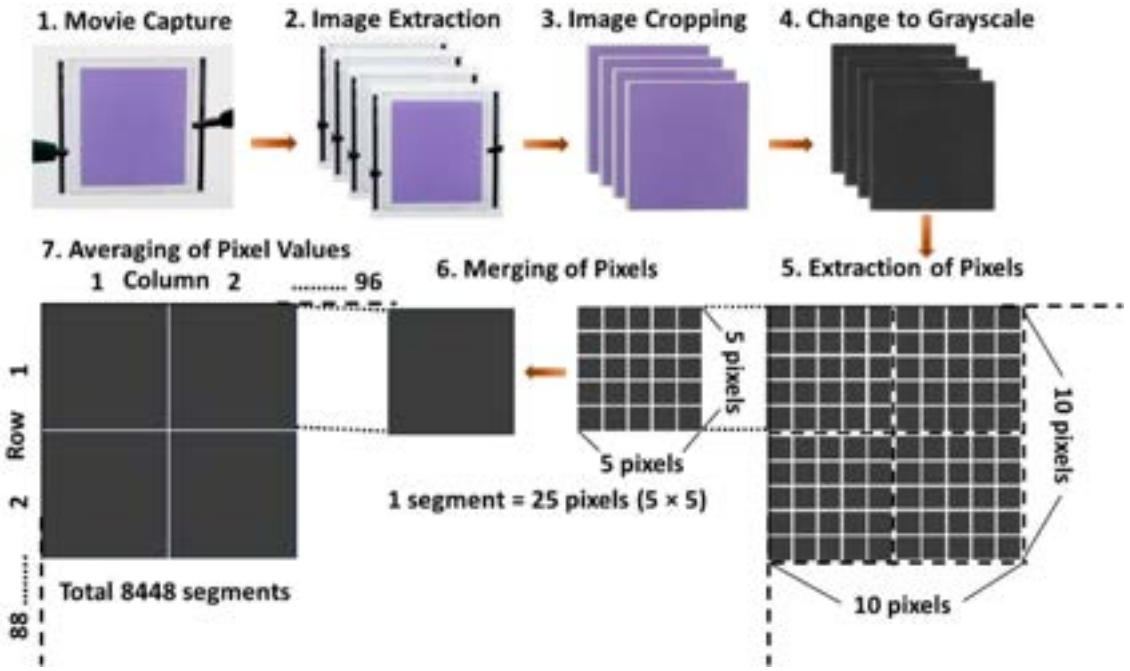

pixel values, a total of 8448 segments (consisting of 96 columns and 88 rows) were obtained for the EC active area of the device (Scheme 1). Consistent lighting conditions and camera settings were maintained throughout this experiment to ensure the reproducibility of the results.

Visualization of Switching Nonuniformity. To assess the EC change quantitatively, the reaction time required to reach 90% of the total contrast change was calculated for every pixel position within the entire EC active area, resulting in a data set covering 8,448 individual segments. The reaction times ranged from 0.8 to 2.0 s, providing a comprehensive evaluation of switching speed across the device. The results are visualized as a two-dimensional heatmap (Figure 2), where each segment is color-coded according to its individual reaction time, with the accompanying color bar depicting the overall reaction time distribution across the device. In this heatmap, the light gray regions correspond to shorter reaction times (faster EC transitions, ≈0.80−1.40 s), indicating a higher device efficiency in these areas. Conversely, the dark gray regions signify longer reaction times (up to ≈2.00 s), representing slower EC responses. This pixel-level kinetic mapping provides a comprehensive visualization of the spatially resolved EC response and allows identification of areas with varying switching behavior. Such analysis provides valuable insight into the spatial uniformity of grayscale image contrast changes, serving as a proxy for optical contrast, across large-area ECDs.

Segmental Kinetic Study on EC Changes. Optical property variations of the ECD were assessed by tracking grayscale contrast values (30 = dark gray, 240 = light gray) over time for a selected segment, E (pixel coordinates (45, 46)), located at the device center. Grayscale intensity served as a direct proxy for optical contrast, enabling quantitative monitoring of dynamic color changes during the switching process. A sequence of grayscale images collected between 0 and 2.5 s (Figure 3a) visually captures the progressive transition from the initial dark, colored state (Fe^{2+}) to the light gray (bleached), colorless state (Fe^{3+}). At 0 s, the selected segment appeared dark, reflecting its fully colored state. After 1.5 s, the segment appeared nearly colorless, and by 2.0 s, the bleaching process was essentially complete. The corresponding contrast−time profile (Figure 3b) numerically represents this change, clearly showing that the grayscale intensity increased from ∼56 in the fully colored state at 0 s to about 214 in the fully bleached state at 2.0 s. The shape of the contrast evolution curve reveals a smooth, sigmoidal transition, with the main intensity change occurring between 0.5 and 1.5 s before approaching saturation near the maximum contrast level. To quantify the switching kinetics, the reaction time was defined as the time required to achieve 90% of the total contrast change. For this central segment E, the switching time was determined to be 1.8 s, as indicated by the red dashed line in Figure 3b. This analysis reveals the localized EC switching behavior of the ECD in the central area, showcasing the time-dependent grayscale contrast changes.

To examine localized EC switching behavior, multiple pixel positions (segments) were selected along a horizontal line of the device for detailed image-based analysis. This approach enabled precise, pixel-level determination of reaction times associated with the $Fe^{2+} \rightarrow Fe^{3+}$ oxidation process, allowing detection of subtle spatial variations across the device. Five representative positions (A−E), distributed from the edge to the center, were identified in the grayscale map of ECD (Figure 4a), and their corresponding reaction times were determined from contrast−time responses (Figure 4b) and summarized in Table S1. The edge segment (A) exhibited a fast reaction time of 1.1 s, whereas the central segment (E) showed slow switching time of 1.8 s, with intermediate positions (B−D) displaying gradually increasing times. This systematic trend indicates a progressive increase in switching time from the edge toward the center. These results demonstrate the capability of the image-based analytical method to resolve spatial heterogeneities in EC switching

https://doi.org/10.1021/acsaelm.5c01754
ACS Appl. Electron. Mater. 2025, 7, 10651−10663

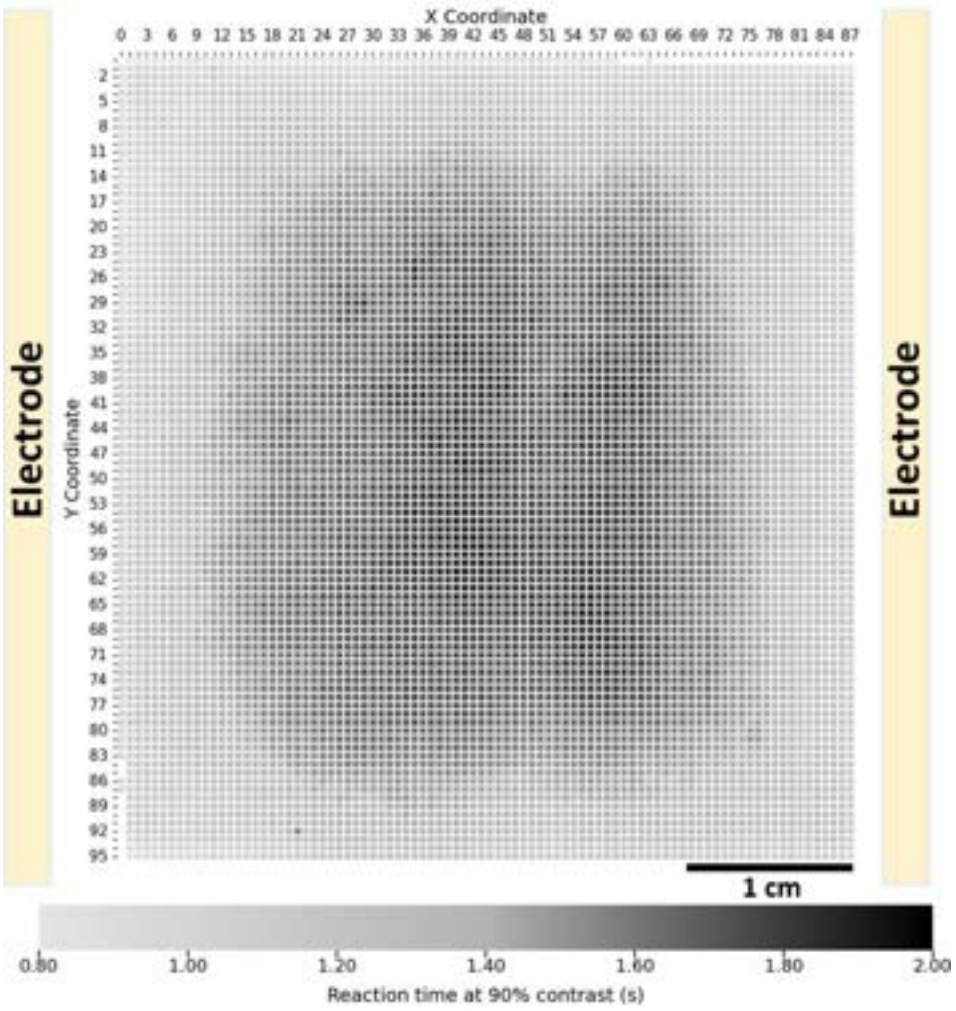

Figure 2. Grayscale heat map visualization of reaction times to reach 90% contrast change for all 8,448 segments of the ECD. The color scale ranges from 0.8 to 2.0 s, representing reaction time, with light gray (0.8−1.4 s) indicating faster EC switching and dark gray (1.8−2.0 s) indicating slower transitions.

behavior and establish a foundation for mapping localized resistance variations within the ECD.

The EC switching dynamics of the device were analyzed using an equivalent-circuit approach adapted from the conceptual framework proposed by Ho and coworkers,[48,49] who demonstrated that large-area ECDs operated under potentiostatic control can be represented by a dominant capacitance in series with an effective resistance that incorporates electrolyte resistance, electrode resistance, charge-transfer resistance, and ionic mass-transport resistance. In such systems, the double-layer capacitance at the electrode/electrolyte interface is much smaller than the working electrode capacitance, allowing the device to be approximated as a single "large capacitor" connected in series with a lumped resistance. This simplified treatment has been widely applied for evaluating EC behavior because it provides direct insight into time-dependent switching characteristics without requiring full impedance deconvolution.[57]

The overall capacitance of the present device was determined from chronoamperometric measurement performed under a 1.2 V potentiostatic step (Figure S1). The resulting current decay profile was fitted with a single exponential function:

$$y = A_1 \times \exp(-x/t_1) + y_0 \quad (1)$$

where t_1 is the characteristic time constant of the RC circuit. From the best fit, the amplitude (A_1) was determined to be 1.13506, and t_1 was 0.29688. Since $A_1 = V/R$ and $V = 1.2$ V, the overall device resistance (R) was calculated as 1.057 Ω. Using the RC relationship ($t_1 = R \times C$), the total device capacitance (C) was obtained as 0.28087 F. Given the device's EC active area of 21.12 cm^2, the capacitance per unit area was calculated as 0.0133 F/cm^2.

In the subsequent spatial analysis, this derived areal capacitance was assumed to be uniform across the device and used to convert the local time constants (τ) into resistance values according to (eq 2). This assumption is reasonable for uniformly processed thin-film devices and was necessary because the image-based contrast−time data do not allow independent extraction of both C and R at each segment. Moreover, experimentally, the **polyFeL1** film exhibited uniform coloration, indicating homogeneous metal (Fe) distribution in the MSP and minimal variation in film thickness; therefore, capacitance variation across the device is expected to be negligible. By fixing C, local resistance variations could be isolated and quantified using

https://doi.org/10.1021/acsaelm.5c01754
ACS Appl. Electron. Mater. 2025, 7, 10651−10663

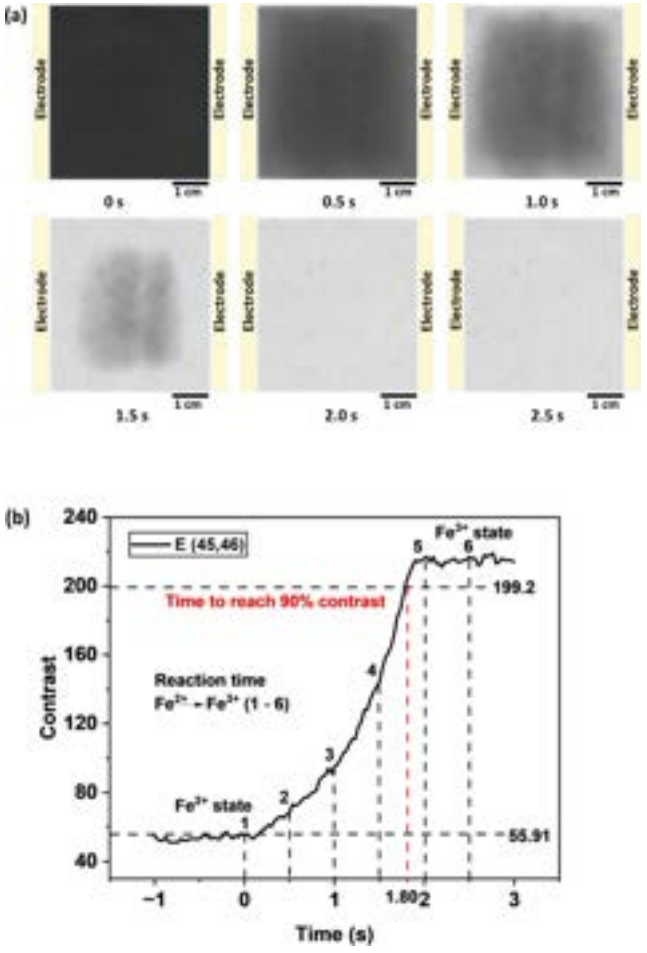

Figure 3. Color-changing rate of a central segment (pixel coordinates x, y: 45, 46) as shown in the form of (a) grayscale images over time (0−2.5 s) illustrate the transition to the colorless state, and (b) the corresponding contrast vs time plot quantifies this change, with the 90% contrast change defining the reaction time (1.8 s) for the central position.

$$R_{segment} = \tau / C \tag{2}$$

where τ is the local time constant determined from a stretched exponential fit of the contrast−time profile (Figure 5d):

$$y = y_0 + A \times (1 - \exp(-((x - x_0)/\tau)^{\beta})) \tag{3}$$

Here, y_0 is the initial contrast, A is the total contrast change, x_0 is the initial time, and β is the stretched exponent obtained from nonlinear curve fitting of the contrast−time data, where both τ and β were treated as free parameters and refined by minimizing the residual sum of squares. The fitting was carried out in OriginPro using initial guesses of τ = 1 s and β = 0.5, and the final β values were extracted directly from the best-fit curves.

This segmental resistance is a composite parameter representing contributions from the ITO electrode resistances, ionic resistance within the polymer gel electrolyte, and charge-transfer resistances at both the NiHCF counter electrode and **polyFeL1** working electrode (Figure 5b). Following the analytical concept proposed by Ho,[48] these contributions are represented as a single effective series resistance (Figure 5c):

$$R_{segment} = R_{ITO} + R_{ct,CM} + R_{ion} + R_{ct,Polymer} + R_{ITO} \tag{4}$$

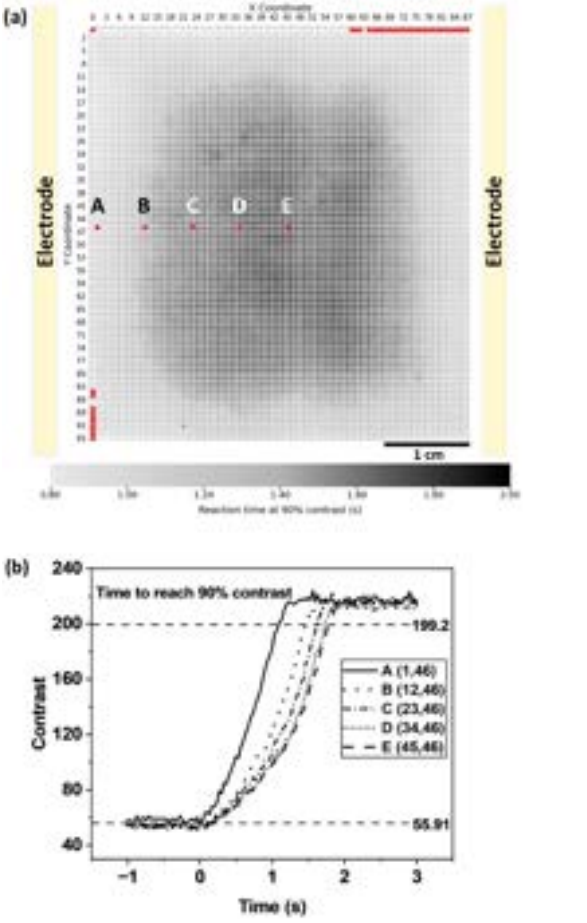

Figure 4. (a) Grayscale map of the ECD, with red-colored pixel coordinates (X, Y) at the edges indicating regions responsible for the high contrast (≥84) values: (0, 0), (0, 84), (0, 85), (0, 88)−(0, 95), and (60, 0)−(87, 0), excluding (63, 0) and five pixel positions (A−E) selected along a horizontal line at Y = 46 in this grayscale map, spanning from the device edge to the center: A (1, 46), B (12, 46), C (23, 46), D (34, 46), and E (45, 46). These positions were chosen to capture spatial variations in device response from the periphery (A, near the busbar) through intermediate regions (B−D) to the central region (E). (b) Corresponding contrast−time responses (−1 to 3 s) for these positions reveal progressively increasing reaction times from A to E and with changes in pixel intensity.

Although these components can be resolved by electrochemical impedance spectroscopy, previous work has shown that for potentiostatically switched devices, the transient behavior is dominated by the working electrode capacitance, making it valid to represent them as one effective term.[48] This approach enables rapid, spatially resolved mapping of electrochemical resistance without location-specific impedance measurements.

Time constants (τ) extracted for five representative pixel positions (edge, intermediate, center) (Figure S2) were obtained by fitting the corresponding contrast−time profiles using eq 3, which provided excellent agreement with the experimental data (R^2 = 0.93−0.99, reduced $\chi^2 \leq 350$). Attempts to fit the same data using single- or double-exponential models resulted in poor convergence and unrealistic τ values, confirming that only the stretched-exponential model adequately represents the experimental kinetics. The extracted τ values were then converted to segmental resistances using eq 2, and the results are

https://doi.org/10.1021/acsaelm.5c01754
ACS Appl. Electron. Mater. 2025, 7, 10651−10663

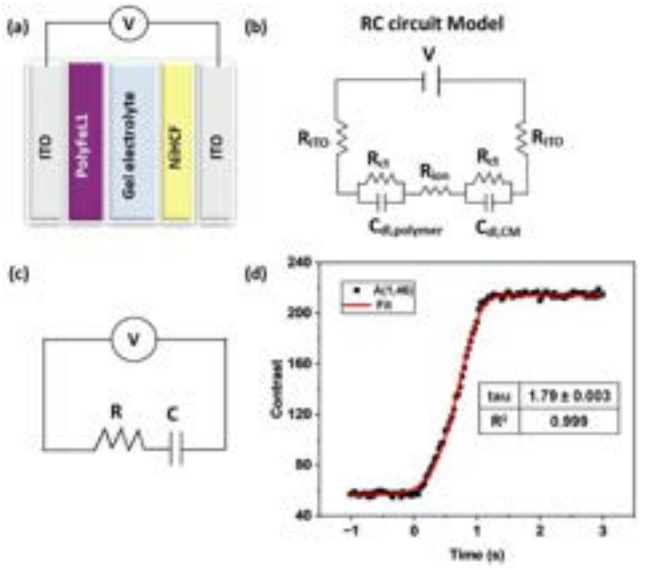

Figure 5. Determination of the local resistance of each segment (pixel position) in the ECD. (a) Layer configuration of the ECD consisting of ITO/**polyFeL1**/gel electrolyte/NiHCF/ITO, (b) representation of the device as a generalized RC circuit, (c) simplified RC representation for local resistance extraction, and (d) nonlinear curve fitting of the time-dependent grayscale contrast at segment A (1, 46), used to extract the time constant (τ) associated with the EC switching process.

summarized in Table 1. Position A, located near the device edge, exhibited a small τ value (1.79), corresponding to a low

Table 1. Summary of the τ Values and Segmental Resistances

Pixel position	Tau value (τ)	Resistance, $R_{segment}$ ($\Omega \cdot cm^2$)
A (1, 46)	1.79 ± 0.003	134.5
B (12, 46)	1.81 ± 0.03	136.1
C (23, 46)	2.13 ± 0.02	160.1
D (34, 46)	2.42 ± 0.01	181.9
E (45, 46)	2.46 ± 0.01	184.9

resistance value (134.5 $\Omega \cdot cm^2$), whereas position E, at the device center, displayed a large τ (2.46), corresponding to a high resistance (184.9 $\Omega \cdot cm^2$). These results reveal a clear spatial gradient in resistance, with slow switching toward the center of the device. The initial grayscale contrast averaged 55.99 ± 3.48, indicating small variability likely arising from optical factors (focus or illumination) or slight thickness differences. Based on this ± 3.48 (≈6%) variation in contrast, a ± 6% sensitivity analysis was performed, producing only proportional shifts in resistance values without altering the overall spatial trend (Table S3). Although minor film-thickness or morphological differences may exist, but are expected to have a negligible influence. Future spatially resolved impedance or SECM mapping will be conducted to experimentally verify local capacitance uniformity.

To further clarify the physical meaning of the obtained resistance values, $R_{segment}$ represents an effective series resistance that combines electronic, ionic, and interfacial contributions within the device. The sheet resistance of the ITO used in the device was 8−10 Ω/sq, and the measured two-probe resistance at ten different distances from the Ag bar on the ITO electrode ranged from 5.1 to 5.3 Ω (average = 5.3 ± 0.06 Ω; Figure S3), indicating that the electronic component of the ITO layer is minor compared with the total areal resistance (134−185 $\Omega \cdot cm^2$) extracted from the image analysis. The PMMA/$LiClO_4$ gel electrolyte typically exhibits ionic conductivities of 10^{-4}−10^{-3} S cm^{-1} at room temperature,[50] consistent with ionic and charge-transfer limitations observed in large-area ECD. Thus, the spatial variations in $R_{segment}$ primarily reflect differences in ionic transport through the gel and charge-transfer processes at the electrode interfaces. Future studies will employ regional electrochemical impedance spectroscopy (EIS) at selected distances to separate these components and verify the spatial interpretation of $R_{segment}$.

The observed spatial nonuniformity is more plausibly attributed to variations in ionic conductivity within the PMMA-based gel electrolyte. Previous studies have shown that ion mobility in PMMA/$LiClO_4$ gels strongly depends on polymer segmental flexibility and solvent content.[50,51] In the present device, the gel layer near the edges likely remains softer and more plasticized, whereas the central region becomes relatively compact and rigid after thermal conditioning, leading to slower ion motion and higher resistance at the center.[52,53] This explanation is consistent with reported decreases in ionic conductivity for more rigid PMMA matrices.[51,54] However, this interpretation remains speculative; other factors, such as slight nonuniformity in film thickness, small ITO sheet-resistance gradients, may also contribute.

Visualization of Spatial Distributions in Switching Dynamics. The color-changing pattern across the EC active area of the **polyFeL1**-based ECD was subsequently evaluated by plotting the corresponding contrast vs time curves for all 8448 segments (Figure 6a). During the transition from purple to colorless under the applied potential, the contrast increased from 25 (black/dark gray) to 250 (white/light gray) in a grayscale spectrum, with a key transition phase occurring

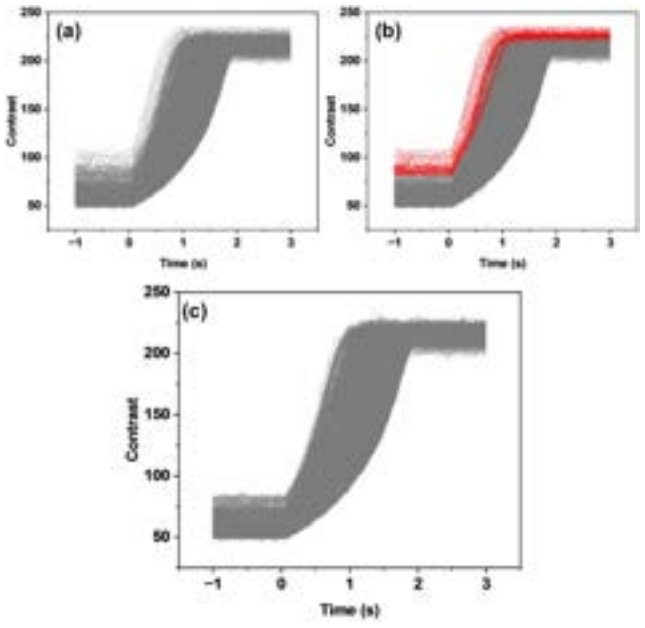

Figure 6. (a) Contrast vs time plot for all 8,448 segments of the ECD. (b) Corresponding plot highlighting segments with unusually high contrast values (≥84, range 84−105), shown in red. (c) Contrast−time plot after removal of these high-contrast segments.

https://doi.org/10.1021/acsaelm.5c01754
ACS Appl. Electron. Mater. 2025, 7, 10651−10663

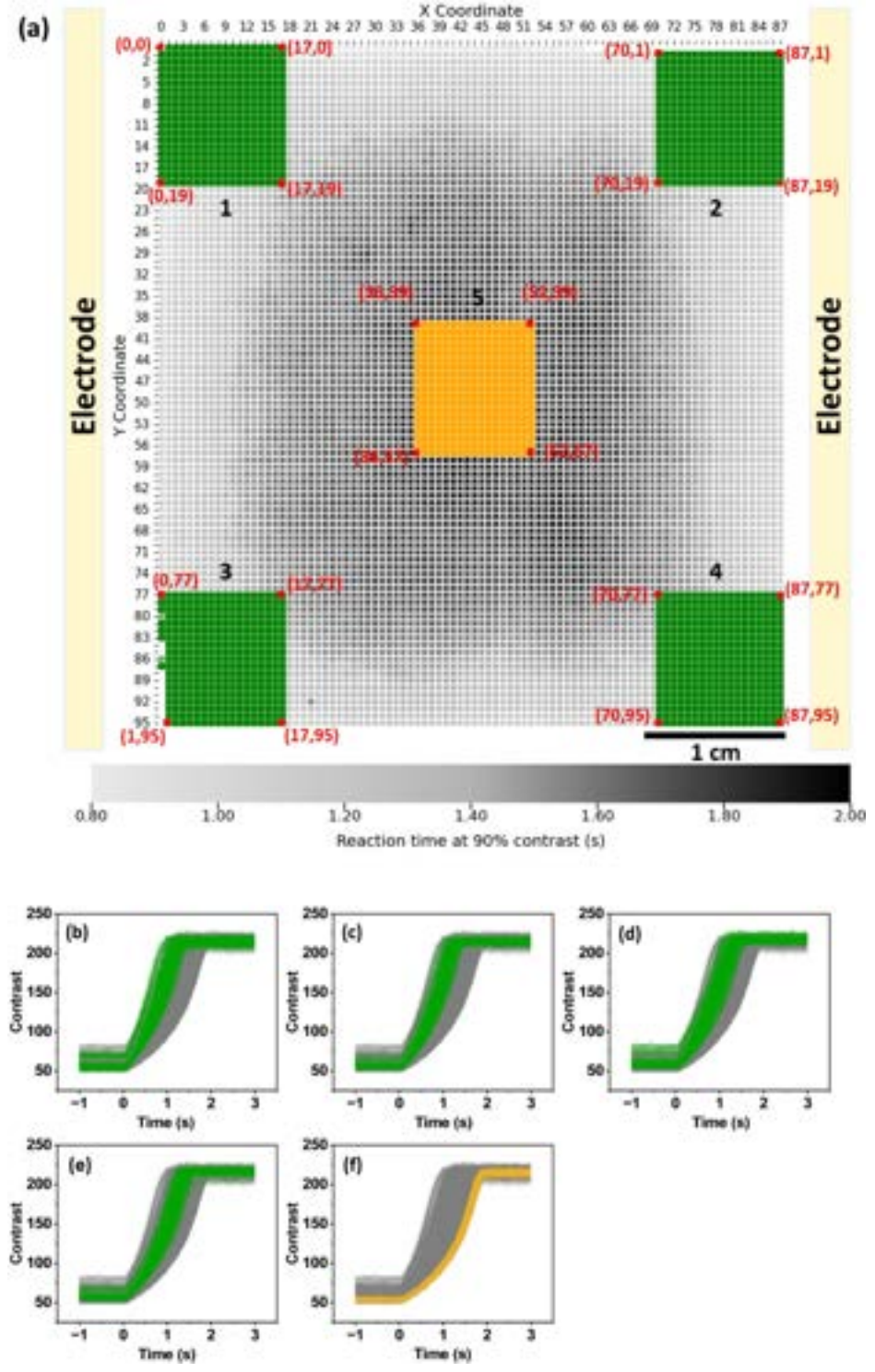

Figure 7. (a) Grayscale map of the ECD with five defined regions of interest selected for spatial switching analysis: four peripheral corner regions (1−4, green) and one central region (5, orange). Each region is indicated by four red (X, Y) corner coordinates: region 1 = (0, 0), (17, 0), (0, 19), (17, 19); region 2 = (70, 1), (87, 1), (70, 19), (87, 19); region 3 = (0, 77), (17, 77), (1, 95), (17, 95); region 4 = (70, 77), (87, 77), (70, 95), (87, 95); region 5 = (36, 39), (52, 39), (36, 57), (52, 57). (b−f) Corresponding contrast−time profiles (−1 to 3 s) illustrate spatial variations in switching kinetics, with faster transitions in the peripheral regions (b−e) and slower responses in the central region (f).

between 0 and 3 s. The initial time (0 s) is the time at which the voltage was applied. Although the device reached a fully transparent state under 2.0 s, the contrast progression exhibited spatial nonuniformity during this period. Initially, the contrast increased sharply, indicating a fast EC response, but a gradual transition followed this, reflected as a curving trend in the contrast vs time plot. Additionally, some higher contrast values (≥84, range 84−105) appeared as noise (Figure 6b), particularly from the pixel coordinates located in the peripheral regions, as shown in Figure 4a, and this was attributed to optical artifacts introduced during video acquisition, most likely caused by a focus gradient or lens

https://doi.org/10.1021/acsaelm.5c01754
ACS Appl. Electron. Mater. 2025, 7, 10651−10663

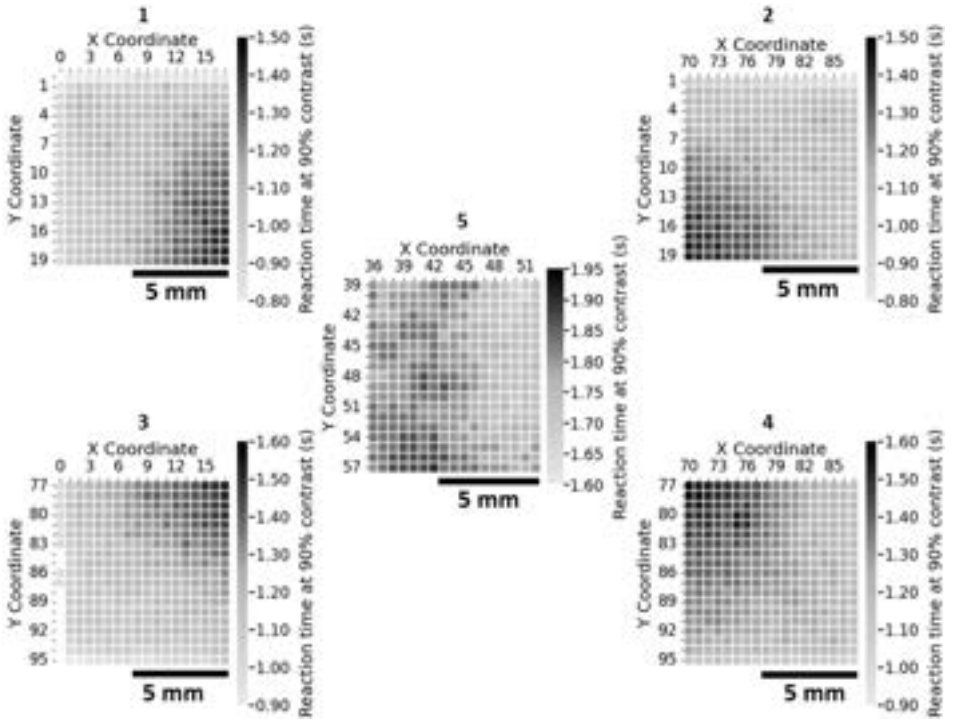

Figure 8. Heat map visualization of the reaction times required to reach 90% contrast change for five defined regions of the ECD: four corner regions (1−4) and one central region (5). The pixel ranges (X, Y) used to define each region are as follows: region 1 = (0−17, 0−19), region 2 = (70−87, 1−19), region 3 = (0−17, 77−95), region 4 = (70−87, 77−95), and region 5 = (36−52, 39−57). The color bars (0.8−1.95 s) represent the reaction-time scale. The heat map highlights spatial differences in switching behavior, with faster response observed in the peripheral corner regions (0.8−1.6 s) and slower switching in the central region (1.6−1.95 s).

distortion in the digital microscope system. These edge-related irregularities were then removed, resulting in a more refined contrast vs time graph (Figure 6c), which accurately represented the true EC response of the device.

To better understand the spatial variation in the EC response, the device was first divided into five vertical regions (columns 1−5) and five horizontal regions (rows 1−5), each represented in distinct colors. The contrast evolution for these vertical regions, relative to the overall device behavior, is shown in Figure S4 through color-coded contrast−time profiles. The reaction times (90% contrast change) were calculated for each region and visualized using 2D heatmaps. In the vertical analysis (Figure S5), columns 1 and 5, corresponding to the left and right edge regions, exhibited fast EC transition with similar reaction times ranging from 0.8 to 1.7 s. In contrast, the central columns (2, 3, and 4) displayed slow responses with almost similar reaction times ranging from 1.0 to 2.0 s. Similarly, in the horizontal analysis (Figures S6 and S7), rows 1 and 5 (apricot and pink), corresponding to the top and bottom edge regions, respectively, showed faster responses with reaction times of 0.8 to 1.7 s and 0.9 to 1.8 s. The central rows 2, 3, and 4 (green, periwinkle, and yellow) exhibited slower responses with reaction times between 1.0 and 2.0 s. This consistent trend across both vertical and horizontal divisions highlights distinct spatial variations, with the edges exhibiting faster switching dynamics than the central regions.

Based on the results from the vertical and horizontal analyses, the device was further subdivided into five discrete regions for more localized analysis: four peripheral corner regions (1−4, green) and one central region (5, orange), as shown in Figure 7a. The contrast dynamics for each region were assessed by plotting contrast−time profiles (Figure 7b−f), providing a clear comparison of switching behavior across the device. Reaction times to reach 90% contrast were calculated for each region and visualized as 2D heat maps (Figure 8). The four corners exhibited similar EC responses, with maximum reaction times of 1.5−1.6 s, indicating consistent and efficient switching across these peripheral zones. In contrast, the central region displayed a broader and longer reaction time range of 1.6−1.95 s, reflecting slower $Fe^{2+} \rightarrow Fe^{3+}$ transitions in this area. The average τ and R values for each region were obtained using the same nonlinear curve fitting method described earlier, summarized in Table 2.

Table 2. Summary of the Average τ and R Values at Regions 1−5 (Corners and Center)

Region	Average tau value (τ)	Average resistance, R ($\Omega \cdot cm^2$)
1	1.82 ± 0.12	136.8
2	1.86 ± 0.09	139.8
3	1.92 ± 0.11	144.4
4	1.99 ± 0.09	149.6
5	2.47 ± 1.81	185.7

Among the corner regions, region 1 showed the lowest average resistance (136.8 $\Omega \cdot cm^2$) along with a faster reaction time range (0.8−1.5 s), whereas the central region exhibited the highest average resistance (185.7 $\Omega \cdot cm^2$), correlating with its slower switching behavior.

To further examine the spatial characterization, the four regions immediately adjacent to the central area were analyzed separately (highlighted in green in the grayscale map of the ECD in Figure S8), along with their corresponding contrast−

https://doi.org/10.1021/acsaelm.5c01754
ACS Appl. Electron. Mater. 2025, 7, 10651−10663

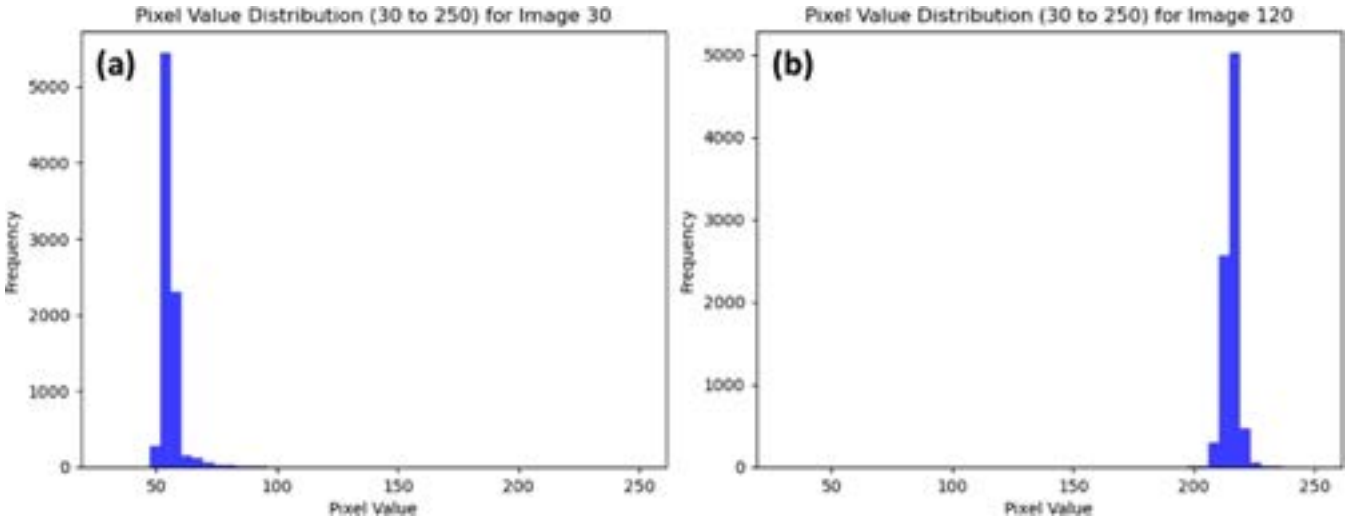

Figure 9. Pixel distribution histograms recorded at (a) 0 s and (b) 3 s during the EC transition from a purple to a colorless state. The *X*-axis represents grayscale brightness (pixel value), and the *Y*-axis indicates pixel frequency. The shift of the intensity peak from the low-brightness range (~45−70) at 0 s to the high-brightness range (~200−230) at 3 s confirms the complete EC transition of the device.

time profiles, to investigate whether they acted as transitional zones between the high-performing edges and the slower-reacting center. The spatial heat maps of reaction times are shown in Figure S9, and the average τ and R values for these intermediate regions are summarized in Table S4. These adjacent regions exhibited intermediate behavior, with reaction times ranging from 1.5 to 1.85 s, average τ values between 2.31 and 2.39, and moderate resistances of 173.7−179.7 $\Omega \cdot cm^2$. The data suggest that these transitional zones bridge the gap between the low-resistance, fast-switching corners and the high-resistance, slower central area, providing further insight into the spatial gradients in switching kinetics and resistance variation within the device.

Artifact Filtering and Validation. High-contrast segments caused by optical artifacts (e.g., focus gradients or lens edge effects) were manually identified and excluded based on their initial grayscale intensity values (≥84, range 84−105). The filtering was performed directly on the Excel data set before further analysis. To confirm that this correction did not influence the quantitative results, the average τ values of two representative corner regions were compared before and after removal of these segments (Table S5). The τ values changed by less than 1%, confirming that artifact filtering had no measurable effect on the overall spatial trend. Representative before-and-after maps are shown in Figure S10.

Overall, the combination of image-based analysis and a simplified RC model provides a rapid and noninvasive method for mapping spatially resolved composite resistances in large ECD. Although the calculated resistances represent a composite of multiple contributions, this approach captures the net EC limitations controlling switching behavior and offers a powerful diagnostic tool for analysis, device design, and process optimization.

Furthermore, to validate the accuracy of the image-based analysis, a comparative measurement was conducted using conventional UV−Vis spectroscopy on a separate **polyFeL1**-based ECD at a wavelength of 580 nm. The transmittance−time response at this wavelength showed a bleaching response time of 4.5 s to achieve 90% optical change. In comparison, the image-based method resolved pixel-level reaction times ranging from 2.0 to 4.25 s for a 90% contrast change (Figure S11). The close agreement between the UV−Vis and image-based results confirms the reliability and effectiveness of the proposed methodology for quantifying EC switching kinetics. Notably, whereas UV−Vis spectroscopy provides information from a small, localized region, the image-based approach enables simultaneous spatiotemporal analysis across the entire device area.

Finally, pixel distribution histograms were constructed (Figure 9) to illustrate the brightness levels (*X*-axis: pixel value) and their respective frequencies (*Y*-axis: frequency) at times of 0 and 3 s during operation of the ECD. At 0 s, the histogram reveals a prominent peak in the lower brightness range (~45−70 pixel value), indicating that the device had not undergone its transition. This was consistent with the expected state of the device before activation. In contrast, at 3 s, the histogram showed a peak in the higher brightness range (~200−230 pixel value), reflecting the completed transition of the EC device to its colorless state. This further confirms the effective transition of the device in response to the applied voltage.

Choice of Segmentation. To evaluate the robustness of the pixel-averaging segmentation, the same data set was reanalyzed with four different averaging windows (1 × 1, 3 × 3, 5 × 5, and 10 × 10 pixels), and the results were summarized in Table S6. As shown in Figure S12, finer segmentations (1 × 1 and 3 × 3) preserved high spatial variation but included significant noise due to pixel-level fluctuations. Increasing the averaging window to 5 × 5 significantly reduced noise while retaining local switching details, and further averaging to 10 × 10 produced overly smoothed profiles, merging neighboring fast and slow regions. The overall switching trend remained consistent across segment sizes 5 × 5 and 10 × 10 (reaction times, 0.8−2.0 s), shown in Figure S13, confirming that the spatial kinetics are robust against segmentation choice. Corresponding τ and R values extracted from representative segments, in Figure S14, followed the same pattern, edge < center (Table S7). However, larger segments showed slightly higher τ and R values due to spatial averaging of mixed domains. Based on this balance between noise suppression and spatial resolution, a 5 × 5 segmentation (8,448 segments, 0.50

https://doi.org/10.1021/acsaelm.5c01754
ACS Appl. Electron. Mater. 2025, 7, 10651−10663

× 0.50 mm area per segment) was selected as optimal for quantitative analysis.

Universality of the Proposed Technique. To validate the general applicability of the image-based method, a Prussian blue (PB)-based ECD (5 × 5 cm^2) was fabricated following the procedure reported by Hara et al. (2008). The EC PB-based device was fabricated using a four-layered structure. The PB layer was prepared by spray-coating an aqueous dispersion of PB nanoparticles (750 μL in 10 mL of water) onto an ITO glass substrate. The spray deposition was performed at a rate of 1 mL min^{-1} for four successive coatings at 95 °C. The device was then assembled by sandwiching the PB-modified ITO working electrode with a blank ITO counter electrode using a UV-curable sealant. After introducing an aqueous electrolyte solution of 0.5 M potassium hydrogen phthalate ($C_8H_5KO_4$) between the electrodes via vacuum suction, the suction ports were sealed with the same sealant and cured under UV light to complete the device (Scheme S2).[56]

The movie of PB-based ECD was recorded at a frame rate of 50 fps during the application of −1.5 to +1.5 V. The pixel-wise grayscale contrast was tracked during the colored-to-colorless transition, and the reaction time at 80% of the total contrast change was extracted (Figure S15), confirming that the analytical method can be applied to other EC materials beyond **polyFeL1**.

CONCLUSIONS

We developed a new noninvasive and automated spatially resolved image-based methodology for the first time and succeeded in analyzing the ECD by tracking and quantifying EC changes at the pixel level. The method enabled evaluation of segmental kinetics, uniformity, and spatial distributions in the ECD. First, switching nonuniformity was visualized by segmenting grayscale images, extracted from video recordings at 0.0333 s intervals, into 8,448 localized pixel positions. Pixel-wise contrast−time profiles revealed reaction times ranging from 0.8 to 2.0 s to reach 90% contrast change. Second, segmental kinetics were evaluated by extracting time constants (τ) through fitting each contrast−time profile with a stretched exponential function, which revealed spatial variations in switching across the device. These τ values were then converted into composite segmental resistances using a simplified RC model with a uniform areal capacitance of 0.0133 F cm^{-2}. At the central pixel position E, the delayed switching (1.8 s) was associated with a large τ (2.46) and high resistance (184.9 Ω·cm^2), highlighting the correlation between local kinetics and resistance. Finally, the spatial distribution of the ECD was visualized and quantified through 2D heat maps of switching time and resistance. The central region exhibited slower responses (1.6−1.95 s) and higher resistances (regional average 185.7 Ω·cm^2, whereas the peripheral regions showed faster transitions (0.8−1.6 s) with lower resistances (136.8−149.6 Ω·cm^2). These trends highlight the influence of ionic redistribution during thermal conditioning and lateral potential gradients associated with ITO resistance.

This approach provides a high-resolution, noninvasive diagnostic platform for mapping localized EC dynamics in large-area ECDs. Beyond **polyFeL1**-based devices, the image-based methodology is broadly applicable to diverse EC systems—including solution-processed, hybrid, and solid-state architectures—where spatial variations in electrode conductivity, electrolyte distribution, and ion mobility govern switching behavior. Future efforts will extend this approach to multiple samples and repeated switching cycles to evaluate reproducibility, device-to-device variability, and long-term operational stability, as well as to monitor environmental degradation, thereby supporting the development of durable, uniform, and scalable EC technologies for smart windows and energy-efficient applications.

ASSOCIATED CONTENT

Supporting Information

The Supporting Information is available free of charge at https://pubs.acs.org/doi/10.1021/acsaelm.5c01754.

Supplementary figures, tables, and schemes showing device fabrication steps, microscope imaging conditions, grayscale image-analysis workflow, segmentation robustness, stretched-exponential fitting results, UV−Vis validation, and reaction-time maps for **polyFeL1**- and Prussian blue-based ECDs (PDF)

AUTHOR INFORMATION

Corresponding Author

Masayoshi Higuchi − *Electronic Functional Macromolecules Group, National Institute for Materials Science (NIMS), Tsukuba, Ibaraki 305-0044, Japan; Graduate School of Information Science and Technology, University of Osaka, Suita, Osaka 565-0871, Japan;* orcid.org/0000-0001-9877-1134; Phone: +81-29-860-4744; Email: HIGUCHI.Masayoshi@nims.go.jp; Fax: +81-29-860-4721

Authors

Shifa Sarkar − *Electronic Functional Macromolecules Group, National Institute for Materials Science (NIMS), Tsukuba, Ibaraki 305-0044, Japan; Graduate School of Information Science and Technology, University of Osaka, Suita, Osaka 565-0871, Japan*

Takefumi Yoshida − *Faculty of Systems Engineering, Wakayama University, Wakayama 640-8510, Japan;* orcid.org/0000-0003-3479-7890

Banchhanidhi Prusti − *Electronic Functional Macromolecules Group, National Institute for Materials Science (NIMS), Tsukuba, Ibaraki 305-0044, Japan;* orcid.org/0000-0003-4489-2509

Satya Ranjan Jena − *Electronic Functional Macromolecules Group, National Institute for Materials Science (NIMS), Tsukuba, Ibaraki 305-0044, Japan*

Kuo-Chuan Ho − *Institute of Polymer Science and Engineering, National Taiwan University, Taipei 10617, Taiwan;* orcid.org/0000-0001-7501-1271

Complete contact information is available at: https://pubs.acs.org/10.1021/acsaelm.5c01754

Notes

The authors declare no competing financial interest.

ACKNOWLEDGMENTS

This research work was financially supported by the Mirai Project (grant number: JPMJMI21I4) from the Japan Science and Technology Agency (JST), in addition to an Environment Research and Technology Development Fund (ERTDF) (JPMEERF20221M02) from the Environmental Restoration and Conservation Agency (ERCA), Japan.

■ ABBREVIATIONS

MSPs, metallosupramolecular polymers; EC, electrochromic; ECDs, electrochromic devices; **PolyFeL1**, Fe(II)-based metallosupramolecular polymer; WE, working electrode; CE, counter electrode; RH, relative humidity

■ REFERENCES

(1) Rosseinsky, D. R.; Mortimer, R. J. Electrochromic Systems and the Prospects for Devices. *Adv. Mater* **2001**, *13* (11), 783−793.

(2) Higuchi, M. Stimuli-Responsive Metallo-Supramolecular Polymer Films: Design, Synthesis and Device Fabrication. *J. Mater. Chem. C* **2014**, *2* (44), 9331−9341.

(3) Schott, M.; Lorrmann, H.; Szczerba, W.; Beck, M.; Kurth, D. G. State-of-the-Art Electrochromic Materials Based on Metallo-Supramolecular Polymers. *Sol. Energy Mater. Sol. Cells* **2014**, *126*, 68−73.

(4) Mondal, S.; Chandra Santra, D.; Ninomiya, Y.; Yoshida, T.; Higuchi, M. Dual-Redox System of Metallo-Supramolecular Polymers for Visible-to-Near-IR Modulable Electrochromism and Durable Device Fabrication. *ACS Appl. Mater. Interfaces* **2020**, *12* (52), 58277−58286.

(5) Fan, H.; Wei, W.; Hou, C.; Zhang, Q.; Li, Y.; Li, K.; Wang, H. Wearable Electrochromic Materials and Devices: From Visible to Infrared Modulation. *J. Mater. Chem. C* **2023**, *11* (22), 7183−7210.

(6) Hsu, C.-Y.; Zhang, J.; Sato, T.; Moriyama, S.; Higuchi, M. Black-to-Transmissive Electrochromism with Visible-to-Near-Infrared Switching of a Co(II)-Based Metallo-Supramolecular Polymer for Smart Window and Digital Signage Applications. *ACS Appl. Mater. Interfaces* **2015**, *7* (33), 18266−18272.

(7) Lu, H.-C.; Hsiao, L.-Y.; Kao, S.-Y.; Seino, Y.; Santra, D. C.; Ho, K.-C.; Higuchi, M. Durable Electrochromic Devices Driven at 0.8 V by Complementary Chromic Combination of Metallo-Supramolecular Polymer and Prussian Blue Analogues for Smart Windows with Low-Energy Consumption. *ACS Appl. Electron. Mater* **2021**, *3* (5), 2123−2135.

(8) Mortimer, R. J.; Dyer, A. L.; Reynolds, J. R. Electrochromic Organic and Polymeric Materials for Display Applications. *Displays* **2006**, *27* (1), 2−18.

(9) Eh, A. L.-S.; Chen, J.; Yu, S. H.; Thangavel, G.; Zhou, X.; Cai, G.; Li, S.; Chua, D. H. C.; Lee, P. S. A Quasi-Solid-State Tristate Reversible Electrochemical Mirror Device with Enhanced Stability. *Adv. Sci* **2020**, *7* (13), 1903198.

(10) Zhang, J.; Jena, S. R.; Higuchi, M. Flexible Multicolor Rewritable Paper Coated with Metallosupramolecular Polymers for Electrochromic Printing and Natural Erasing by Humidity. *ACS Appl. Polym. Mater* **2023**, *5* (9), 6950−6957.

(11) Azens, A.; Avendaño, E.; Backholm, J.; Berggren, L.; Gustavsson, G.; Karmhag, R.; Niklasson, G.; Roos, A.; Granqvist, C. Flexible Foils with Electrochromic Coatings: Science, Technology and Applications. *Mater. Sci. Eng. B* **2005**, *119*, 214−223.

(12) Wang, Z.; Zhu, H.; Zhuang, J.; Lu, Y.; Chen, Z.; Guo, W. Recent Advance in Electrochromic Materials and Devices for Display Applications. *ChemPlusChem* **2024**, *89*, No. e202300770.

(13) Byker, H. J. Electrochromics and Polymers. *Electrochim. Acta* **2001**, *46* (13), 2015−2022.

(14) Jelle, B.; Hagen, G. Transmission Spectra of an Electrochromic Window Based on Polyaniline, Prussian Blue and Tungsten Oxide. *J. Electrochem. Soc* **1993**, *140*, 3560−3564.

(15) Mortimer, R. J. Electrochromic Materials. *Chem. Soc. Rev* **1997**, *26* (3), 147−156.

(16) Granqvist, C. G. Electrochromic Tungsten Oxide Films: Review of Progress 1993−1998. *Sol. Energy Mater. Sol. Cells* **2000**, *60* (3), 201−262.

(17) Gaupp, C.; Welsh, D.; Rauh, R.; Reynolds, J. Composite Coloration Efficiency Measurements of Electrochromic Polymers Based on 3,4-Alkylenedioxythiophenes. *Chem. Mater* **2002**, *14*, 3964−3970.

(18) Lu, H.-C.; Kao, S.-Y.; Chang, T.-H.; Kung, C.-W.; Ho, K.-C. An Electrochromic Device Based on Prussian Blue, Self-Immobilized Vinyl Benzyl Viologen, and Ferrocene. *Sol. Energy Mater. Sol. Cells* **2016**, *147*, 75−84.

(19) Santra, D. C.; Mondal, S.; Yoshida, T.; Ninomiya, Y.; Higuchi, M. Ru(II)-Based Metallo-Supramolecular Polymer with Tetrakis(N-Methylbenzimidazolyl)Bipyridine for a Durable, Nonvolatile, and Electrochromic Device Driven at 0.6 V. *ACS Appl. Mater. Interfaces* **2021**, *13* (26), 31153−31162.

(20) Mondal, S.; Roy, S.; Fujii, Y.; Higuchi, M. Highly Durable Electrochromic Devices for More than 100,000 Cycles with Fe(II)-Based Metallo-Supramolecular Polymer by Optimization of the Device Conditions. *ACS Appl. Electron. Mater* **2023**, *5* (12), 6677−6685.

(21) Hu, C.-W.; Sato, T.; Zhang, J.; Moriyama, S.; Higuchi, M. Multi-Colour Electrochromic Properties of Fe/Ru-Based Bimetallo-Supramolecular Polymers. *J. Mater. Chem. C* **2013**, *1* (21), 3408−3413.

(22) Mondal, S.; Yoshida, T.; Maji, S.; Ariga, K.; Higuchi, M. Transparent Supercapacitor Display with Redox-Active Metallo-Supramolecular Polymer Films. *ACS Appl. Mater. Interfaces* **2020**, *12* (14), 16342−16349.

(23) Guo, J.; Jia, H.; Shao, Z.; Jin, P.; Cao, X. Fast-Switching WO_3-Based Electrochromic Devices: Design, Fabrication, and Applications. *Acc. Mater. Res* **2023**, *4* (5), 438−447.

(24) Higuchi, M.; Kurth, D. G. Electrochemical Functions of Metallosupramolecular Nanomaterials. *Chem. Rec* **2007**, *7* (4), 203−209.

(25) Wang, Y.; Shen, R.; Wang, S.; Zhang, Y.-M.; Zhang, S. X.-A. Dynamic Metal−Ligand Interaction of Synergistic Polymers for Bistable See-Through Electrochromic Devices. *Adv. Mater* **2022**, *34* (8), 2104413.

(26) Granqvist, C. G.; Arvizu, M. A.; Bayrak Pehlivan, İ.; Qu, H.-Y.; Wen, R.-T.; Niklasson, G. A. Electrochromic Materials and Devices for Energy Efficiency and Human Comfort in Buildings: A Critical Review. *Electrochim. Acta* **2018**, *259*, 1170−1182.

(27) Casini, M. Smart windows for energy efficiency of buildings. *International Journal of Civil and Structural Engineering− IJCSE* **2015**, *2*, 230−238.

(28) Wu, S.; Sun, H.; Duan, M.; Mao, H.; Wu, Y.; Zhao, H.; Lin, B. Applications of Thermochromic and Electrochromic Smart Windows: Materials to Buildings. *Cell Rep. Phys. Sci* **2023**, *4* (5), 101370.

(29) In, Y.; Kim, Y. M.; Lee, Y.; Choi, W.; Kim, S.; Lee, S.-W.; Moon, H. Ultra-Low Power Electrochromic Heat Shutters Through Tailoring Diffusion-Controlled Behaviors. *ACS Appl. Mater. Interfaces* **2020**, *12* (27), 30635−30642.

(30) Tripathi, M. K.; Kumar, R.; Tripathi, R. Big-Data Driven Approaches in Materials Science: A Survey. *Mater. Today: Proc* **2020**, *26*, 1245−1249.

(31) Liu, Y.; Zhao, T.; Ju, W.; Shi, S. Materials Discovery and Design Using Machine Learning. *J. Materiomics* **2017**, *3* (3), 159−177.

(32) Siva, P. N.; Yamaganti, D.; Rohita; Sikharam, U. m. *A Review on Python for Data Science, Machine Learning and IOT*. Kharkiv National University of Radio Electronics 2023. .

(33) Kalidindi, S. R.; De Graef, M. Materials Data Science: Current Status and Future Outlook. *Annu. Rev. Mater. Res* **2015**, *45*, 171−193.

(34) Himanen, L.; Geurts, A.; Foster, A. S.; Rinke, P. Data-Driven Materials Science: Status, Challenges, and Perspectives. *Adv. Sci* **2019**, *6* (21), 1900808.

(35) Ramaripa, P. S.; Modibane, K. D.; Seleka, W. M.; Somo, T. R.; Makhado, E.; Makgopa, K.; Ogunbayo, T. B. Recent Applications of Analytical Techniques and Electrochemical Methods in Characterizations of the Titanium Dioxide Composites. *Int. J. Electrochem. Sci* **2024**, *19* (1), 100444.

(36) Balaji, S.; Djaoued, Y.; Albert, A.-S.; Ferguson, R. Z.; Brüning, R. Hexagonal Tungsten Oxide Based Electrochromic Devices: Spectroscopic Evidence for the Li Ion Occupancy of Four-Coordinated Square Windows. *Chem. Mater* **2009**, *21* (7), 1381−1389.

(37) Shkirskiy, V.; Kang, M.; McPherson, I. J.; Bentley, C. L.; Wahab, O. J.; Daviddi, E.; Colburn, A. W.; Unwin, P. R.

https://doi.org/10.1021/acsaelm.5c01754
ACS Appl. Electron. Mater. 2025, 7, 10651−10663

Electrochemical Impedance Measurements in Scanning Ion Conductance Microscopy. *Anal. Chem* **2020**, *92* (18), 12509−12517.
(38) Granqvist, C. G.; Lansåker, P. C.; Mlyuka, N. R.; Niklasson, G. A.; Avendaño, E. Progress in Chromogenics: New Results for Electrochromic and Thermochromic Materials and Devices. *Sol. Energy Mater. Sol. Cells* **2009**, *93* (12), 2032−2039.
(39) Assis, L. M. N.; Andrade, J. R.; dos Santos, L. H. E.; Motheo, A. J.; Hajduk, B.; Lapkowski, M.; Pawlicka, A. Spectroscopic and Microscopic Study of Prussian Blue Film for Electrochromic Device Application. *Electrochim. Acta* **2015**, *175*, 176−183.
(40) Mondal, S.; Yoshida, T.; Rana, U.; Bera, M. K.; Higuchi, M. Thermally Stable Electrochromic Devices Using Fe(II)-Based Metallo-Supramolecular Polymer. *Sol. Energy Mater. Sol. Cells* **2019**, *200*, 110000.
(41) Sudheeshna, M.; Malarvannan, M.; Kumar, K. V.; Kumar, G. K.; Reddy, Y. P. 2D Chromatography and 2D Spectroscopy in Analytical Chemistry: An Overview. *J. Anal. Chem* **2023**, *78* (9), 1213−1230.
(42) O'Sullivan, E. M.; Grobert, N.; Swart, M. Density Functional Theory Investigation of 2D Phase Separated Graphene/Hexagonal Boron Nitride Monolayers: Band Gap, Band Edge Positions, and Photoactivity. *J. Phys. Chem. C* **2025**, *129*, 638−664.
(43) Guillén, E.; Ferrer-Roselló, M.; Agrisuelas, J.; García-Jareño, J. J.; Vicente, F. Digital Video-Electrochemistry (DVEC) to Assess Electrochromic Materials in the Frequency Domain: RGB Colorimetry Impedance Spectroscopy. *Electrochim. Acta* **2021**, *366*, 137340.
(44) Agrisuelas, J.; García-Jareño, J. J.; Perianes, E.; Vicente, F. Use of RGB Digital Video Analysis to Study Electrochemical Processes Involving Color Changes. *Electrochem. Commun* **2017**, *78*, 38−42.
(45) Athane, A. P.; Prasad, S. R. Image Enhancement Based on OpenCV Using Python.7 − Review. *Int. Adv. Res. J. Sci. Eng. Technol* **2021**, *8* (5), 429−436.
(46) Guillen, G. Digital Image Processing with Python and OpenCV. In *Sensor Projects with Raspberry Pi*; Springer: Apress, Berkeley, CA, 2019, pp. 97−140. .
(47) Tan, L.; Jiang, J. Chapter 14 - Image Processing Basics. In *Digital Signal Processing*, 2nd ed.; Tan, L.; Jiang, J.; Eds.; Academic Press: Boston, 2013; pp. 683−765. .
(48) Ho, K.-C. Cycling Stability of an Electrochromic System at Room Temperature. *J. Electrochem. Soc* **1992**, *139* (4), 1099−1104.
(49) Ho, K.-C.; Rukavina, T. G.; Greenberg, C. B. Tungsten Oxide−Prussian Blue Electrochromic System Based on a Proton-Conducting Polymer Electrolyte. *J. Electrochem. Soc* **1994**, *141* (8), 2061−2067.
(50) Appetecchi, G. B.; Croce, F.; Scrosati, B. Kinetics and Stability of the Lithium Electrode in Poly(methyl methacrylate)-Based Gel Electrolytes. *Electrochim. Acta* **1995**, *40* (8), 991−997.
(51) Kaur, D. P.; Yamada, K.; Park, J.-S.; Sekhon, S. S. Correlation between Ion Diffusional Motion and Ionic Conductivity for Different Electrolytes Based on Ionic Liquid. *J. Phys. Chem. B* **2009**, *113* (16), 5381−5390.
(52) Chen, T.; Zhao, F.; Wang, L.; Ma, S.; Shi, G.; Liu, Q.; Liu, Y.; Han, G. High-Performance PMMA-Based Solvent-Free Solid Transparent Polymer Electrolyte Modified by Succinonitrile for Electrochromic Devices. *Sol. Energy Mater. Sol. Cells* **2025**, *285*, 113538.
(53) Abdelhamed, A. H. E.; Thien, G. S. H.; Lee, C.-L.; Au, B. W.-C.; Tan, K. B.; Murthy, H. C. A.; Chan, K.-Y. Solution Casting Effect of PMMA-Based Polymer Electrolyte on the Performances of Solid-State Electrochromic Devices. *Polymers* **2025**, *17* (1), 99.
(54) Guan, X.; Chen, F.; Li, Z.; Zhou, H.; Ma, X. Influence of a Rigid Polystyrene Block on the Free Volume and Ionic Conductivity of a Gel Polymer Electrolyte Based on Poly(methyl methacrylate)-block-polystyrene. *J. Appl. Polym. Sci* **2016**, *133* (22), 43901.
(55) Sarkar, S.; Sakata, K.; Fujii, Y.; Higuchi, M. Large Device Fabrication of Electrochromic Smart Windows with Fe(II)-Based Metallosupramolecular Polymer. *ITE Trans. Media Technol. Appl* **2025**, *13* (4), 364−371.
(56) Hara, S.; Shiozaki, H.; Omura, A.; Tanaka, H.; Kawamoto, T.; Tokumoto, M.; Yamada, M.; Gotoh, A.; Kurihara, M.; Sakamoto, M. Color-Switchable Glass and Display Devices Fabricated by Liquid Processes with Electrochromic Nanoparticle "Ink. *Appl. Phys. Express* **2008**, *1* (10), 104002.
(57) Kuo, T.-J.; Lee, K.-Y.; Huang, C.-K.; Chen, J.-H.; Chiu, W.-L.; Huang, C.-F.; Wu, S.-D. State of Charge Modeling of Lithium-Ion Batteries Using Dual Exponential Functions. *J. Power Sources* **2016**, *315*, 331−338.

https://doi.org/10.1021/acsaelm.5c01754
ACS Appl. Electron. Mater. 2025, 7, 10651−10663